Biophysical Journal
Article

Biophysical Society

Response of Single Cells to Shock Waves and Numerically Optimized Waveforms for Cancer Therapy

Dongli Li,[1,*] Antonio Pellegrino,[1] Andre Hallack,[1] Nik Petrinic,[1] Antoine Jérusalem,[1,*] and Robin O. Cleveland[1,*]
[1]Department of Engineering Science, University of Oxford, Oxford, United Kingdom

ABSTRACT Shock waves are used clinically for breaking kidney stones and treating musculoskeletal indications. The mechanisms by which shock waves interact with tissue are still not well understood. Here, ultra-high-speed imaging was used to visualize the deformation of individual cells embedded in a tissue-mimicking phantom when subject to shock-wave exposure from a clinical source. Three kidney epithelial cell lines were considered to represent normal healthy (human renal epithelial), cancer (CAKI-2), and virus-transformed (HK-2) cells. The experimental results showed that during the compressive phase of the shock waves, there was a small (<2%) decrease in the projected cell area, but during the tensile phase, there was a relatively large (~10%) increase in the projected cell area. The experimental observations were captured by a numerical model with a constitutive material framework consisting of an equation of state for the volumetric response and hyper-viscoelasticity for the deviatoric response. To model the volumetric cell response, it was necessary to change from a higher bulk modulus during the compression to a lower bulk modulus during the tensile shock loading. It was discovered that cancer cells showed a smaller deformation but faster response to the shock-wave tensile phase compared to their noncancerous counterparts. Cell viability experiments, however, showed that cancer cells suffered more damage than other cell types. These data suggest that the cell response to shock waves is specific to the type of cell and waveforms that could be tailored to an application. For example, the model predicts that a shock wave with a tensile stress of 4.59 MPa would increase cell membrane permeability for cancer cells with minimal impact on normal cells.

INTRODUCTION

A shock wave is a type of acoustic wave characterized by the presence of a rapid-pressure jump governed by the interaction of nonlinear effects that steepen the waveform and attenuation mechanisms that smooth the waveform (1). Shock waves have been medically used for decades in a procedure called lithotripsy, in which shock waves fragment kidney stones. Although lithotripsy is a mature technology, there are concerns about bioeffects, including renal hemorrhage and scarring with a permanent loss of functional renal volume (2,3). Although damage is predominantly thought to be induced by cavitation (4,5) even in environments where cavitation is minimized, damage has been reported in cells (6) and tissues (7), suggesting a direct impact of shock waves on cells.

Shock waves have also been employed for orthotripsy, which is the treatment of musculoskeletal disorders, such as plantar fasciitis, tendon pain, and nonunions or delayed unions of long-bone fractures (8). The mechanism by which shock waves have an effect on musculoskeletal conditions is not understood. One of the hypotheses is that the disruption of the tissue by shock waves results in "microtrauma," which then induces neovascularization that is believed to improve blood supply and tissue regeneration. The increased permeability of the vessel wall may also promote the healing process (8).

Cancer therapy is another field in which shock waves have been investigated (9–11). It has been reported that besides mechanically rupturing cells, shock waves may enhance the sonoporation effect that temporarily increases the membrane permeability to allow molecules in the surrounding medium to diffuse into cells (9). This provides a mechanism for shock-wave-mediated therapeutic drug delivery and gene transfer. Furthermore, some experimental results have shown a positive influence of shock waves on suppressing tumor growth and selectively killing malignant cells (10,11). The mechanisms by which shock waves affect cancer cells are not well understood.

Submitted February 27, 2017, and accepted for publication September 28, 2017.

*Correspondence: dongli.li@eng.ox.ac.uk or antoine.jerusalem@eng.ox.ac.uk or robin.cleveland@eng.ox.ac.uk

Editor: Philip LeDuc.
https://doi.org/10.1016/j.bpj.2017.09.042

All of these applications motivate the need for a better understanding of the interaction between shock waves and cells. The goal of this work is to develop a numerical model for the response of a single cell to shock waves that is calibrated and validated against ultra-high-speed imaging of single-cell deformation under the action of shock waves. The differences in cell response to shock waves due to cell type is also examined. The numerical model employs a three-dimensional (3D) continuum model of an individual cell modeled with a combined equation of state (EoS) and hyper-viscoelastic material framework. The validated numerical model was then used to analyze the development of the stress and strain fields under the compressive and tensile phases of the shock wave, from which insights into the mechanisms of cell destruction and sonoporation were obtained. Two shock-wave profiles are proposed to specifically target cancer cells for enhanced sonoporation or rupture while minimizing impact on normal healthy cells.

MATERIALS AND METHODS

The experimental rig consisted of a shock-wave source coupled to a tissue-mimicking gel in which cells were embedded. The gel contained cell media to maintain cell viability. Three kidney epithelial cell lines representing cancer cells, normal healthy cells, and virus-transformed cells were studied. An ultra-high-speed camera (SIMX 16; Specialised Imaging, Tring, United Kingdom) with a 20× objective (UMPLFLN20XW; Olympus, Tokyo, Japan) was used to image individual cells. Before the cell experiments, the camera and shock source were coaligned with a needle hydrophone.

For each experiment, the camera was focused onto a cell in the focal region of the shock waves. A reference image was taken before the delivery of shock waves. A shock wave was delivered, and the camera was triggered to capture 16 frames at a rate of 3.3 Mfps (interframe time of 300 ns with an exposure time of 200 ns). Each cell was imaged with three different shock-wave energy settings. The imaging experiment was repeated on eight different target cells for each of the three cell lines investigated. Further details of the experimental system are described in the Supporting Material.

The high-speed images were filtered and then processed to extract the boundary of the cells from the images using methods described in the Supporting Material. The deformation of the cell was determined by comparing the cell boundary during shock-wave passage to the cell boundary in the reference image; we note that a separate reference image was used for each camera channel to avoid channel-to-channel differences. Quantitative analysis of the perimeter and area change was performed based on the extracted cell boundaries.

Shock-wave pressure profiles

Fig. 1 shows pressure waveforms measured at the focus of a clinical shock-wave source (Minilith SL1-0G; STORZ, Tuttlingen, Germany) at three different energy settings (levels 4, 6, and 8) using a bespoke fiber-optic probe hydrophone embedded in a tissue-mimicking phantom (12). In each case, the shock wave consists of a compressive phase (duration around 1.5 μs) followed by a tensile phase (duration around 2.1 μs). As the energy level increased, three effects were observed: an increase in the peak positive pressure, a decrease in the shock-rise time (time duration for the shock front pressure to rise from 10 to 90% of the maximal shock pressure), and a gradual increase in the peak negative pressure. These are characteristic behaviors of a focused nonlinear acoustic wave (13).

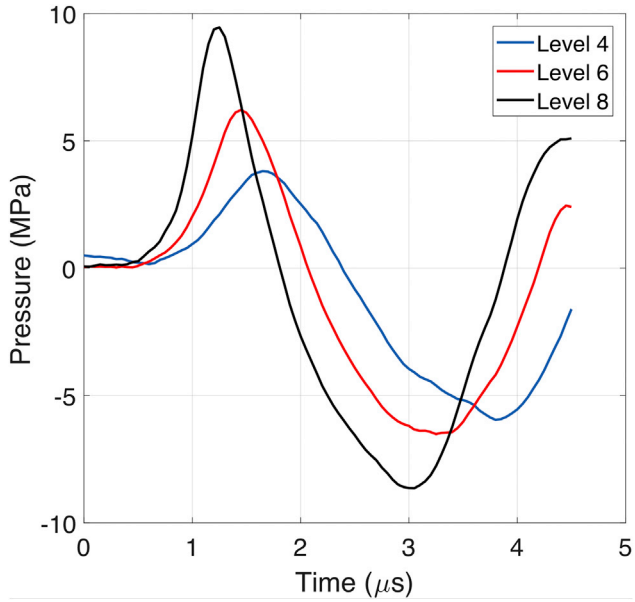

FIGURE 1 Measured focal shock waves in a tissue-mimicking phantom for source energy level 4 (*blue*), level 6 (*red*), and level 8 (*black*). To see this figure in color, go online.

Single-cell deformation under a shock wave

Fig. 2, *a–c* show representative images of an individual healthy human kidney (human renal epithelial (HRE); Lonza, Basel, Switzerland) cell during the compressive phase of a shock wave at energy level 8. The cell boundary was extracted, as described in the Supporting Material, and it can be seen that the cell is translated and the contour is slightly compressed in this phase of the shock wave. Fig. 2, *d–f* show the cell during the tensile phase, and it can be seen that the boundary has expanded and also become more diffuse in the image. As described in the Supporting Material, the effects of variability in the imaging, segmentation, and acousto-optic interactions were analyzed and found not to mask the cell deformation under shock waves.

The projected cell area inside the cell boundary was calculated for every image, and Fig. 3, *a*, *d*, and *g* show the relative area change-time curve (see Eq. 10 in the Supporting Material) for HRE cells for the three shock wave energy settings. It can be seen that the cells initially undergo a small compression (<2% area decrease) followed by a large expansion that increases with the increase of shock-wave energy levels (up to 13% area increase at shock-wave energy level 8). The timing of cell deformation was found to be consistent with the compressive phase and tensile phase of the shock wave; however, the sixfold increase in cell area changes between tension and compression was not consistent with the fact that the magnitude of the tensile stress was comparable to that of compression with similar loading rates. These data suggest that the cells are stiffer during compression than under tension.

The experiments were repeated with virus-transformed immortalized kidney cells (HK-2; ATCC, Manassas, Virginia) (Fig. 3, *b*, *e*, and *h*) and kidney cancer cells (CAKI-2; ATCC, Manassas, Virginia) (Fig. 3, *c*, *f*, and *i*). Both the cancer cells and immortalized cells exhibited the same qualitative behavior as that of the healthy cells (a small response to the compressive phase and a large response to the tensile phase of the shock wave). Further, the cell-area change increased with the shock-wave energy level setting, and the difference in the maximal area increase among the three cell types also became more distinguishable; see Supporting Material. At energy level 8, the maximal area increase was 13% in HRE cells (Fig. 3 *g*), 17% in the HK-2 cells (Fig. 3 *h*), and 9% in CAKI-2 cells (Fig. 3 *i*). The difference was statistically significant for HK-2 and CAKI-2 cells with a *p*-value of less than

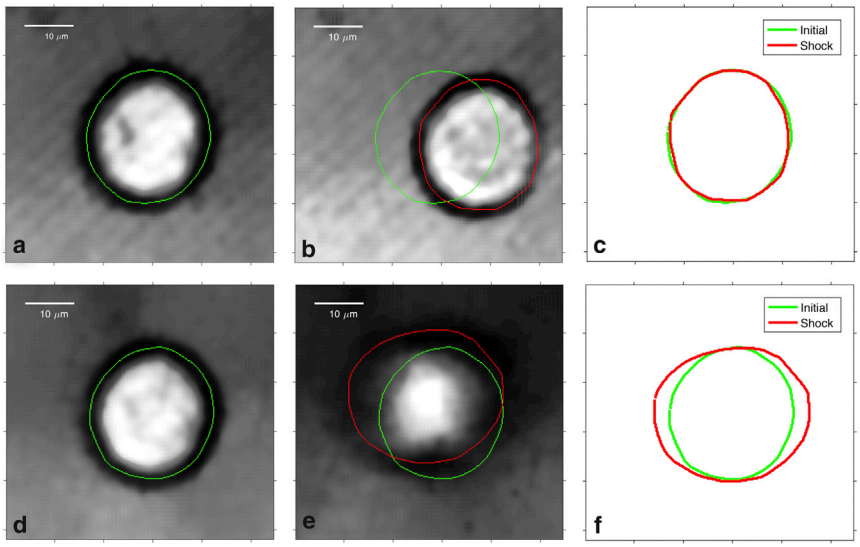

FIGURE 2 Deformation of a healthy HRE cell during the compression phase (*a–c*) and tension phase (*d–f*) at energy level 8. (*a*) and (*d*) depict the cell before the shock wave, (*b*) and (*e*) depict the cell during the shock wave interaction, and (*c*) shows a cell contour comparison before (*green*) and during (*red*) shock wave exposure. To see this figure in color, go online.

0.05 in the Mann-Whitney U test. Furthermore, the duration of cell-area expansion was longer for the CAKI-2 cells (~1.8 μs) than for the HRE and HK-2 cells (~1.5 μs). These results indicate that the CAKI-2 cells exhibit stiffer mechanical characteristics during tension than those of normal or virus-transformed cells. We note that the duration of the tensile deformation of cells was slightly shorter than the 2.1 μs duration of the shock-wave tensile phase, which suggests that there may be a hysteresis effect present in the transition from compression to expansion.

The projected cell area can be thought as a proxy for the volumetric deformation of the cell and the cell perimeter for assessing its deviatoric response. It was found that the ratio of the projected area change to perimeter change for all three cell types at the three different energy-level settings remained between 1.5 and 2, which results in less than a 10% variation from a circular shape (analysis presented in the Supporting Material) and therefore suggests that the cells did not undergo substantial shear deformation during the shock-wave exposure. A measure of shear-related perimeter change was calculated by factoring out the volumetric contribution. It was found that the shear-related perimeter change for all three cell types remained less than 0.5%, further suggesting a small shearing effect in the experiment. More details are provided in the Supporting Material.

Cell viability test

To investigate the difference in cell response to shock waves for different cell types embedded in the agarose gel, a cell viability test was performed using a lactate dehydrogenase assay (ThermoFisher Scientific, Pierce, Waltham, Massachusetts) after shock-wave exposure. Cell viability is determined by light absorbance; to measure a detectable signal, ~500,000 cells were concentrated to the shock-wave focal zone and exposed to 500 shock waves at energy levels 4 and 8. The detailed experimental protocol is explained in the Supporting Material.

Fig. 4 shows the results of cell cytotoxicity after shock-wave exposure at energy levels 4 and 8. It can be seen that at energy level 4, no shock-wave-induced cytotoxicity was observed. The negative values indicate that shock-wave-treated cell samples presented higher cell viability than that of the nontreated sham samples. This effect has been found in previous studies in which lower-amplitude shock waves enhanced cell proliferation (14,15). At energy level 8, all three cell lines exhibited cell cytotoxicity after shock-wave exposure, and the cancer cell line (CAKI-2) suffered higher cytotoxicity compared to the other two normal cell lines (HK-2 and HRE).

Numerical study

The 3D finite element model employed here consisted of a cell surrounded by an extracellular matrix. The deformation was decomposed into a deviatoric response and a volumetric response. The deviatoric response was described by the first-order generalized Maxwell viscoelasticity, which consists of a long-term shear modulus (μ_∞), a viscous shear modulus (μ_1), and a viscosity (η_1) (16). The volumetric response was modeled by a bilinear acoustic EoS that employed different bulk moduli for the compressive and tensile phases of the shock wave with a transition at the early stage of the tensile wave. The surrounding matrix was modeled by nonlinear elasticity in combination with an acoustic EoS.

The measured shock waves (see Fig. 1) were used as boundary conditions for the top surface of the model and propagated as a plane wave through the computational domain. Further details are presented in the Supporting Material.

Numerical model calibration and validation

The mechanical properties of the numerical model under ultra-high strain-rate-loading were calibrated against the experimental measurements of the cell-area change.

Based on the larger deformation observed in the tensile phase than in the compressive phase, a bilinear EoS was proposed to model the volumetric change of a single-cell subject to shock waves. This EoS employs a high bulk modulus in compression and a lower bulk modulus in tension with a transition-pressure threshold to govern the transition between them. The compressive bulk modulus was estimated to be 2 GPa because of the small cell deformation under compression as well as the high water content of the cell (pure water has a bulk modulus of 2.2 GPa (17)). The other two material parameters (i.e., tensile bulk modulus and transition pressure threshold) were calibrated for each cell line by minimizing the least-square error of cell-area change between the simulation and experimental results. The final mechanical properties of the model calibrated across all three shock-wave energy levels are presented in Table 1.

The bulk moduli and transition pressure for HK-2 and HRE cells are similar, whereas the CAKI-2 cells exhibit a higher modulus in tension and a lower transition pressure. The mechanical properties suggest that even though the cancer cells have the largest bulk modulus, the lower transition pressure threshold makes them the first to undergo large deformation during tension.

The simulation results of the cross-sectional area change (which is equivalent to the projected cell area from the experiments) for each cell line using

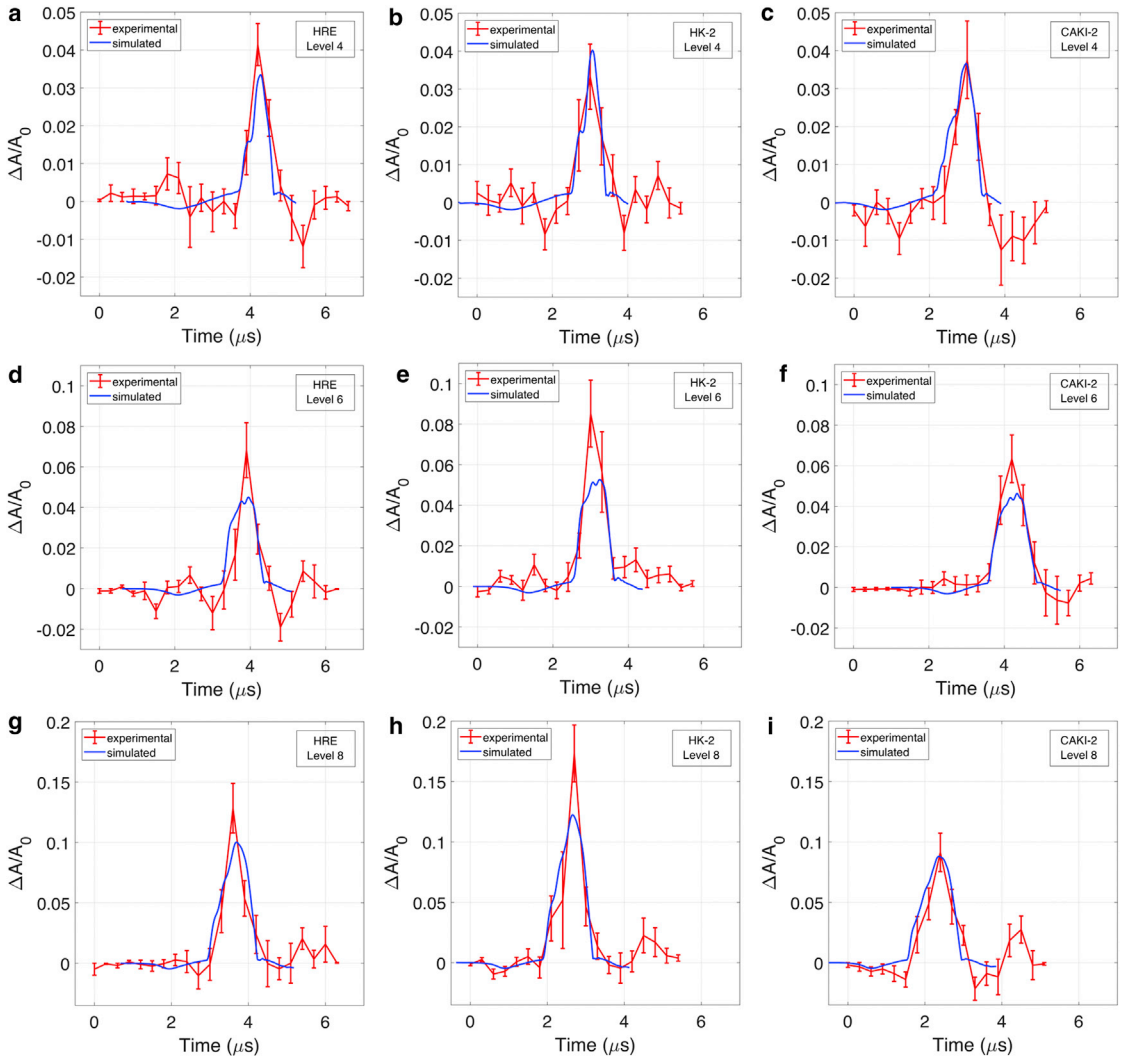

FIGURE 3 Experimental (*red*) and simulation (*blue*) results of cell-area change in response to shock waves. The cell deformation is shown at the following shock-wave energy levels: (*a–c*) level 4, (*d–f*) level 6, (*g–i*) level 8 for HRE (*a*, *d*, and *g*), HK-2 (*b*, *e*, and *h*), and CAKI-2 cells (*c*, *f*, and *i*). The error bar shows the SE based on nine individual cells for each case. To see this figure in color, go online.

the optimized material parameters are presented in blue in Fig. 3. It can be seen that the simulations capture the response across all three energy levels with one unique set of material properties for each cell line. During the calibration process, the influence of the deviatoric material properties (shear moduli and viscosity) on the cell-area change was found to be insignificant (a factor of 10^6 in the deviatoric properties resulted in <0.01% of area change). This is consistent with the experimental observations that the cell response is dominated by its volumetric deformation. The deviatoric properties used in the study were obtained from the literature ($\mu_0 = 3.1$ kPa, $\mu_1 = 0.34$ kPa, $\eta = 69.6$ Pa.s) (18,19).

Quantification of stress and strain evolution of cells

The numerical model quantifies the cell response in terms of stress and strain evolutions in 3D, which provides insights into shock-wave interactions with cells. The shock-wave propagation was found not to be strongly influenced by the difference in mechanical properties between the cell types. The von Mises stress, which quantifies the amount of shearing in the model, was found to be of the order of 100 Pa using the deviatoric mechanical properties from the literature. The overall cell membrane strain $\Delta S/S_0$, which describes the area change of the cell membrane (see Eq. 21 in the Supporting Material), was also analyzed as an indicator of cell-membrane permeability showing the maximal values of 10% in HRE, 12% in HK-2, and 8.5% in CAKI-2 cells at shock-wave energy level 8. More details are provided in the Supporting Material.

Optimization of shock-wave loading

The validated numerical model allows for the testing of designed shock-wave profiles to elicit a specific cell response. For example, a shock wave with a tensile stress of the order of 4.5 MPa will exceed the transition threshold of cancer cells, but not healthy cells, and therefore, it could sonoporate or even rupture cancer cells without damaging normal cells. Fig. 5, *a* and *b* present a proposed shock-wave profile with a peak negative pressure of 4.59 MPa and the predicted membrane strain for each cell type. The difference in the threshold for CAKI-2 and HRE (HK-2) cells resulted in 1.1% of membrane strain in CAKI-2 cells at the maximal tensile pressure, whereas the membrane strain of HK-2 and HRE cells remained less than

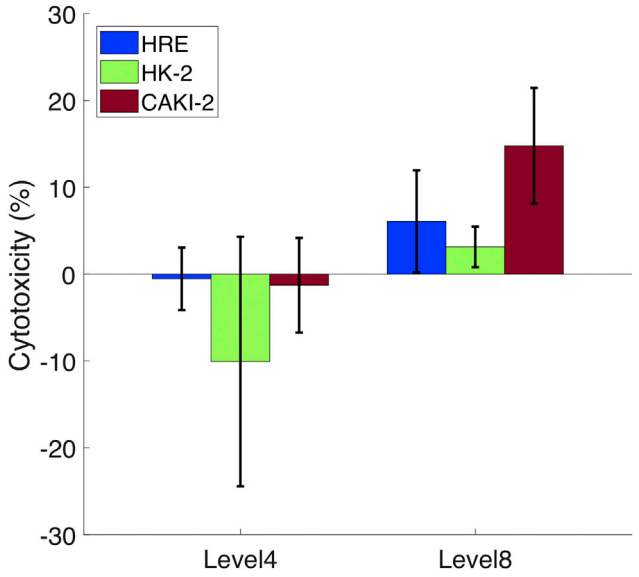

FIGURE 4 Cell cytotoxicity of different cell lines at shock-wave energy levels 4 and 8. The error bar represents the SD calculated from six experimental repeats for each cell line and shock-wave condition. Welch's *t*-tests showed a statistically significant difference between CAKI-2 and HK-2 or HRE ($p < 0.05$). To see this figure in color, go online.

0.2%. The rupture-strain threshold for cancer cells has been reported to be around 5% (20,21); therefore, with 1.1% of tensile membrane strain, increased cell membrane permeability may be expected even though permanent damage may not occur.

Research studies have also shown that the rupture strain threshold is 40% or higher for normal cells (22,23). Therefore, another shock loading with a peak negative pressure of 7 MPa was proposed (see Fig. 5 *c*), and it is expected to result in rupture of cancer cells (>5% membrane-area increase). In this case, the noncancerous cells (HK-2 and HRE cells) showed relatively large deformation during tension (~5.5 and 6.5%, respectively); however, this is still well below the reported rupture threshold for normal cells. In addition, the expansion in cancer cells was longer in duration compared to that of their noncancerous counterparts (HK-2 and HRE cells), which may lead to higher energy deposition for damaging cancer cells.

RESULTS AND DISCUSSION

The key result in this work is that cells subject to shock waves were stiffer under compression (compressive deformation <2%) than under tension (tensile deformation ~10%) even though the compressive phase of the shock wave was comparable to the tensile phase. This phenomenon was captured in the simulation by use of a bilinear model for the bulk modulus in the EoS with a high modulus for compression and a lower modulus for tension with a transition-pressure threshold.

TABLE 1 Mechanical Properties for Different Cell Types

	Compressive	Tensile	Transition
	Bulk Modulus (GPa)	Bulk Modulus (MPa)	Pressure (MPa)
CAKI-2	2	34	−4
HK-2	2	20	−4.6
HRE	2	25	−4.6

Differences in cell deformation under compression and tension have been reported at lower strain rates and are related to the cytoskeletal network, which consists of actin filaments, intermediate filaments, and microtubules bathed in a fluid environment (the cytosol) (24). It has been suggested that actin filaments and intermediate filaments provide resistance to tension (acting like springs), whereas microtubules are resistant to compression (acting like rods) (25). It is thus expected that cells behave differently under different external loadings (e.g., compression versus tension). Furthermore, the observed cell deformation is also consistent with the idea that under compression, the presence of water in the cells results in a bulk modulus similar to that of water. Under tension, the decrease in bulk modulus beyond a critical tensile stress suggests that some combination of mechanical structure failure and fluid cavitation may be at play within the cell. However, in the data shown in Fig. 3, no macroscopic failure or cavitation was directly observed. Possible mechanisms for microrupture include intracellular cavitation in the cytoplasm (26), intramembrane cavitation in which rupture occurs between the layers of the lipids that make up the cell membrane (27), or phase transition of the lipids in the cell membrane from a gel state to a fluid state (28). The presence of large deformation under tension indicates that both cell damage and increased membrane permeability are likely to occur during this stage of the shock loading.

Fitting of the numerical models to the measured cell deformation suggested that CAKI-2 cells have a greater tensile stiffness than that of HK-2 and HRE cells. This contrasts with the general consensus that cancers cells have lower stiffness than normal cells (29,30), although there are also reports of cancer cells having greater stiffness than normal cells (31,32). Additionally, previously reported stiffness values refer to the Young's modulus measured at slow strain rates ($<10\ s^{-1}$), whereas we report the bulk modulus at a very high strain rate ($>10^4\ s^{-1}$), at which a strong strain rate effect is expected. Note also that the bulk modulus and Young's modulus will not be strongly correlated, particularly when the Poisson's ratio is close to 0.5, as is expected for cells.

The cell viability experiments indicate that shock waves at energy level 4 did not result in cell death for any of the cell types. The simulations predicted that the maximal tensile membrane strains of both cancerous and normal healthy cell lines at energy level 4 are less than 4% (Fig. S19 *a*). Previous work has reported that the rupture strain threshold for cancer cells is around 5% (20,21), whereas that of normal cells has been reported to be 40% or higher (22,23). The predicted strains induced by energy level 4 are less than these values (with the caveat that these reports are at low strain rates); therefore, the lack of cell death is consistent with the strains being below the damage threshold. For the experiments at energy level 8, CAKI-2 cells exhibited greater cell

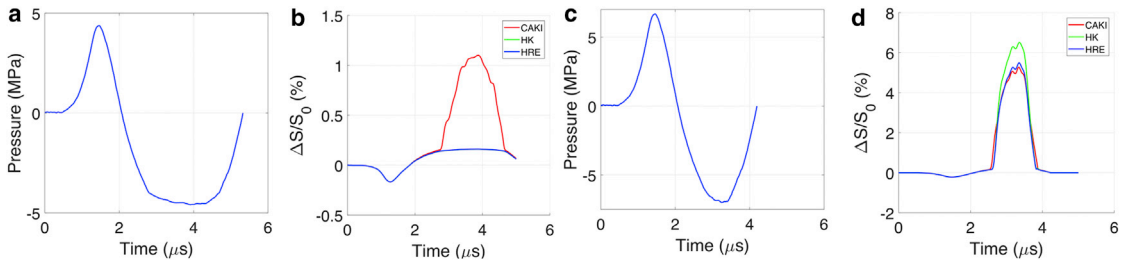

FIGURE 5 (*a*) First proposed shock loading with a maximal tensile pressure of 4.59 MPa. (*b*) The resultant cell membrane strain is shown in three cell types. (*c*) The second proposed shock loading has a maximal tensile pressure of 7 MPa. (*d*) The resultant cell membrane strain is shown in three cell types. To see this figure in color, go online.

toxicity than that of normal cells; this was despite the fact that the larger bulk modulus of the cancerous cells meant that the simulations predicted that the CAKI-2 cells should experience a peak tensile membrane strain (8%, Fig. S19 *c*) that is smaller than that of normal cells (>10%, Fig. S19 *a*). The difference is consistent with the reports that cancerous cells are more fragile than normal cells and that this effect is more important than the change in the bulk modulus.

These results motivated the design of shock-wave profiles to specifically target cancer cells for therapy without affecting normal cells. The first was designed to facilitate sonoporation into cancer cells by employing a shock wave with a peak tensile pressure of −4.59 MPa, which should exceed the transition pressure threshold of cancer cells (−4 MPa), but not that of normal cells (−4.6 MPa). The results from the simulations, depicted in Fig. 5, *a* and *b*, predicted a 1.1% membrane strain increase for CAKI-2 cells as opposed to 0.2% found for the HK-2 and HRE cells. The strain in the CAKI-2 cells should be sufficient to result in cell membrane permeability without inducing cell death and without any effect on healthy cells. The second designed shock-wave profile employed a higher tensile pressure and resulted in >5% membrane strain in cancer cells (Fig. 5, *c* and *d*) for cancer-cell rupture, whereas the predicted membrane stretch was of ∼5% in normal cells; these strains should result in cell death for CAKI-2 cells (which are more fragile) while leaving normal cells intact.

We acknowledge that the experimental setup employed here does not fully capture in vivo conditions. Embedding cells in transparent gel allowed for the visualization and study of single-cell deformation under shock waves in the presence of a scaffold that captures the bulk mechanical properties of tissue. Ideally, the cells under investigation would be in contact with their surroundings; however, this setup is crucial to study cell behavior at the cellular and subcellular levels (e.g., therapeutic molecules permeating cell membranes).

In conclusion, to our knowledge, this work reports the first quantitative combination of experimental measurements and numerical simulations of the deformation of single cells in response to shock waves. The experimental results showed that the dominant response of the cells was during the tensile phase of the shock waves with a tensile strain of ∼10% for a peak tensile pressure around −8 MPa. A bilinear bulk modulus with tensile transition stress was used to capture the observed asymmetry between compression and tension. The experiments and simulations suggest that cell damage or sonoporation effects occur during the tensile phase even though the pressure magnitude is greater during compression. The numerical model was then used to identify shock-wave profiles that can differentiate the tensile responses between cancer cells and noncancerous cells to achieve cancer-cell-specific therapy: sonoporation and cell damage.

SUPPORTING MATERIAL

Supporting Materials and Methods, 19 figures, and one table are available at http://www.biophysj.org/biophysj/supplemental/S0006-3495(18)30205-4.

ACKNOWLEDGMENTS

The authors thank James Fisk, David Salisbury, and Steven Ramsay for their technical support on the design and manufacture of experimental devices; Specialised Imaging Ltd. for providing and supporting us with the lighting for high-speed imaging; Dr. Phillip A. Anderson and Dr. Hugo Doyle for providing and supporting us with the customized fiberoptic probe hydrophone measurement; Emily Kwong for helping with the experiments; and Prof. Robert Carlisle and Dr. Sandra Nwokeoha for helping with the cell culture.

D.L. gratefully acknowledges funding from the Research Councils UK Digital Economy Programme grant number EP/G036861/1 (Oxford Centre for Doctoral Training in Healthcare Innovation). R.C. and D.L. acknowledge the Oxford Centre for Drug Delivery Devices (OXCD3) under grant EP/L024012/1. A.J. and D.L. acknowledge funding from the European Research Council under the European Union's Seventh Framework Programme (FP7 2007–2013)/European Research Council Grant Agreement No. 306587. The research data supporting this publication may be accessed through the Oxford University Research Archive (https://ora.ox.ac.uk).

REFERENCES

1. Cleveland, R. O., and J. A. McAteer. 2012. The physics of shock-wave lithotripsy. *In* Smith's Textbook of Endourology, Third Edition. Wiley-Blackwell, pp. 529–558.
2. Silberstein, J., C. M. Lakin, and J. Kellogg Parsons. 2008. Shock wave lithotripsy and renal hemorrhage. *Rev. Urol.* 10:236–241.

3. McAteer, J. A., and A. P. Evan. 2008. The acute and long-term adverse effects of shock wave lithotripsy. *Semin. Nephrol.* 28:200–213.
4. Carstensen, E. L., S. Gracewski, and D. Dalecki. 2000. The search for cavitation in vivo. *Ultrasound Med. Biol.* 26:1377–1385.
5. Matlaga, B. R., J. A. McAteer, …, L. R. Willis. 2008. Potential for cavitation-mediated tissue damage in shockwave lithotripsy. *J. Endourol.* 22:121–126.
6. Williams, J. C., Jr., J. F. Woodward, …, J. A. McAteer. 1999. Cell damage by lithotripter shock waves at high pressure to preclude cavitation. *Ultrasound Med. Biol.* 25:1445–1449.
7. Evan, A. P., L. R. Willis, …, L. A. Crum. 2002. Kidney damage and renal functional changes are minimized by waveform control that suppresses cavitation in shock wave lithotripsy. *J. Urol.* 168:1556–1562.
8. Wang, C. J. 2003. An overview of shock wave therapy in musculoskeletal disorders. *Chang Gung Med. J.* 26:220–232.
9. Murata, R., K. Nakagawa, …, H. Moriya. 2007. The effects of radial shock waves on gene transfer in rabbit chondrocytes in vitro. *Osteoarthritis Cartilage.* 15:1275–1282.
10. Gamarra, F., F. Spelsberg, …, A. E. Goetz. 1993. Complete local tumor remission after therapy with extra-corporeally applied high-energy shock waves (HESW). *Int. J. Cancer.* 55:153–156.
11. Steinhauser, M. O., and M. Schmidt. 2014. Destruction of cancer cells by laser-induced shock waves: recent developments in experimental treatments and multiscale computer simulations. *Soft Matter.* 10:4778–4788.
12. Parsons, J. E., C. A. Cain, and J. B. Fowlkes. 2006. Cost-effective assembly of a basic fiber-optic hydrophone for measurement of high-amplitude therapeutic ultrasound fields. *J. Acoust. Soc. Am.* 119:1432–1440.
13. Averkiou, M. A., and M. F. Hamilton. 1997. Nonlinear distortion of short pulses radiated by plane and focused circular pistons. *J. Acoust. Soc. Am.* 102:2539–2548.
14. Nwokeoha, S., R. Carlisle, and R. O. Cleveland. 2016. The application of clinical lithotripter shock waves to RNA nucleotide delivery to cells. *Ultrasound Med. Biol.* 42:2478–2492.
15. Weihs, A. M., C. Fuchs, …, D. Rünzler. 2014. Shock wave treatment enhances cell proliferation and improves wound healing by ATP release-coupled extracellular signal-regulated kinase (ERK) activation. *J. Biol. Chem.* 289:27090–27104.
16. Simo, J. C., and T. J. R. Hughes. 2008. Computational Inelasticity, Volume 7. Springer-Verlag, New York.
17. Nave, C. R. 2016. Bulk elastic properties. *In* HyperPhysics. Georgia State University.
18. Jérusalem, A., and M. Dao. 2012. Continuum modeling of a neuronal cell under blast loading. *Acta Biomater.* 8:3360–3371.
19. Rebelo, L. M., J. S. de Sousa, …, M. Radmacher. 2013. Comparison of the viscoelastic properties of cells from different kidney cancer phenotypes measured with atomic force microscopy. *Nanotechnology.* 24:055102.
20. Weiss, L. 1992. Biomechanical interactions of cancer cells with the microvasculature during hematogenous metastasis. *Cancer Metastasis Rev.* 11:227–235.
21. Weiss, L., D. S. Dimitrov, and M. Angelova. 1985. The hemodynamic destruction of intravascular cancer cells in relation to myocardial metastasis. *Proc. Natl. Acad. Sci. USA.* 82:5737–5741.
22. Li, F., C. U. Chan, and C. D. Ohl. 2013. Yield strength of human erythrocyte membranes to impulsive stretching. *Biophys. J.* 105:872–879.
23. Shigematsu, T., K. Koshiyama, and S. Wada. 2015. Effects of stretching speed on mechanical rupture of phospholipid/cholesterol bilayers: molecular dynamics simulation. *Sci. Rep.* 5:15369.
24. Stamenović, D., and N. Wang. 2011. Stress transmission within the cell. *Compr. Physiol.* 1:499–524.
25. Ingber, D. E. 2003. Tensegrity I. Cell structure and hierarchical systems biology. *J. Cell Sci.* 116:1157–1173.
26. Brujan, E. 2010. Cavitation in Non-Newtonian Fluids: With Biomedical and Bioengineering Applications, Volume 7. Springer-Verlag, New York.
27. Krasovitski, B., V. Frenkel, …, E. Kimmel. 2011. Intramembrane cavitation as a unifying mechanism for ultrasound-induced bioeffects. *Proc. Natl. Acad. Sci. USA.* 108:3258–3263.
28. Lewis, R. N. A. H., and R. N. McElhaney. 2012. Membrane lipid phase transitions and phase organization studied by Fourier transform infrared spectroscopy. *Biochim. Biophys. Acta.* 1828:2347–2358.
29. Li, Q. S., G. Y. H. Lee, …, C. T. Lim. 2008. AFM indentation study of breast cancer cells. *Biochem. Biophys. Res. Commun.* 374:609–613.
30. Lekka, M., P. Laidler, …, A. Z. Hrynkiewicz. 1999. Elasticity of normal and cancerous human bladder cells studied by scanning force microscopy. *Eur. Biophys. J.* 28:312–316.
31. Zhang, G., M. Long, …, W.-Q. Yu. 2002. Mechanical properties of hepatocellular carcinoma cells. *World J. Gastroenterol.* 8:243–246.
32. Suresh, S. 2007. Biomechanics and biophysics of cancer cells. *Acta Biomater.* 3:413–438.

Biophysical Journal, Volume *114*

Supplemental Information

Response of Single Cells to Shock Waves and Numerically Optimized Waveforms for Cancer Therapy

Dongli Li, Antonio Pellegrino, Andre Hallack, Nik Petrinic, Antoine Jérusalem, and Robin O. Cleveland

SI: Response of Single Cells to Shock Waves and Numerically Optimized Waveforms for Cancer Therapy

Dongli Li, Antonio Pellegrino, Andre Hallack, Nik Petrinic, Antoine Jérusalem and Robin O. Cleveland

University of Oxford, Department of Engineering Science, Parks Rd., Oxford, OX1 3PJ, UK

1 Experimental setup

The experimental setup is described in Fig. 1, in which individual cells were embedded in a tissue-mimicking sample and their response to shock waves was visualised through an ultra-high speed imaging system.

1.1 Cell and tissue phantom preparation

Three human kidney epithelial cell lines were used in the experiments in order to compare the mechanical properties between invasive cancer cells and their non-cancerous counterparts. Normal cells were represented by human renal epithelial (HRE) cells (CC-2556, Lonza) which are primary cells isolated from human renal cortex and glomerular. Cancer cells were from clear cell carcinoma, CAKI-2 (ATCC HTB-47). Immortalised cells, which were transformed by HPV-16 virus, were used as the third cell line: HK-2 (ATCC CRL-2190). The three cell lines were routinely maintained in their corresponding culture medium in a cell culture incubator: BulletKit human renal cell system (Lonza) was used for HRE cells, McCoy's 5a Medium Modified (ATCC) and DMEM (Life Technology) both supplemented with 10% FBS and 1% antibiotic/antimycotic solution were used for CAKI-2 and HK-2 cells.

The day before experiments, cells from each cell line were trypsinized and resuspended in culture medium to a density of $\sim 0.1 \times 10^6$ cells/mL before being injected into a tissue-mimicking phantom. Each tissue-mimicking phantom consisted of 672 mg purified agarose powder (UltraPure Agarose, Invitrogen), 100 mL phosphate buffered saline (Gibco, ThermoFisher Scientific) and 112 mL of culture medium with resuspended cells ($\sim$1.2 million cells). The mixture was stirred gently at 37 °C and poured into a plexiglass mould, see Fig. 2, to set over 24 hours. The resulting phantoms had an elastic modulus of $\sim$10 kPa, similar to what would be expected for soft tissue [1, 2]. The cell density was chosen so that individual cells could be observed when subject to shock waves.

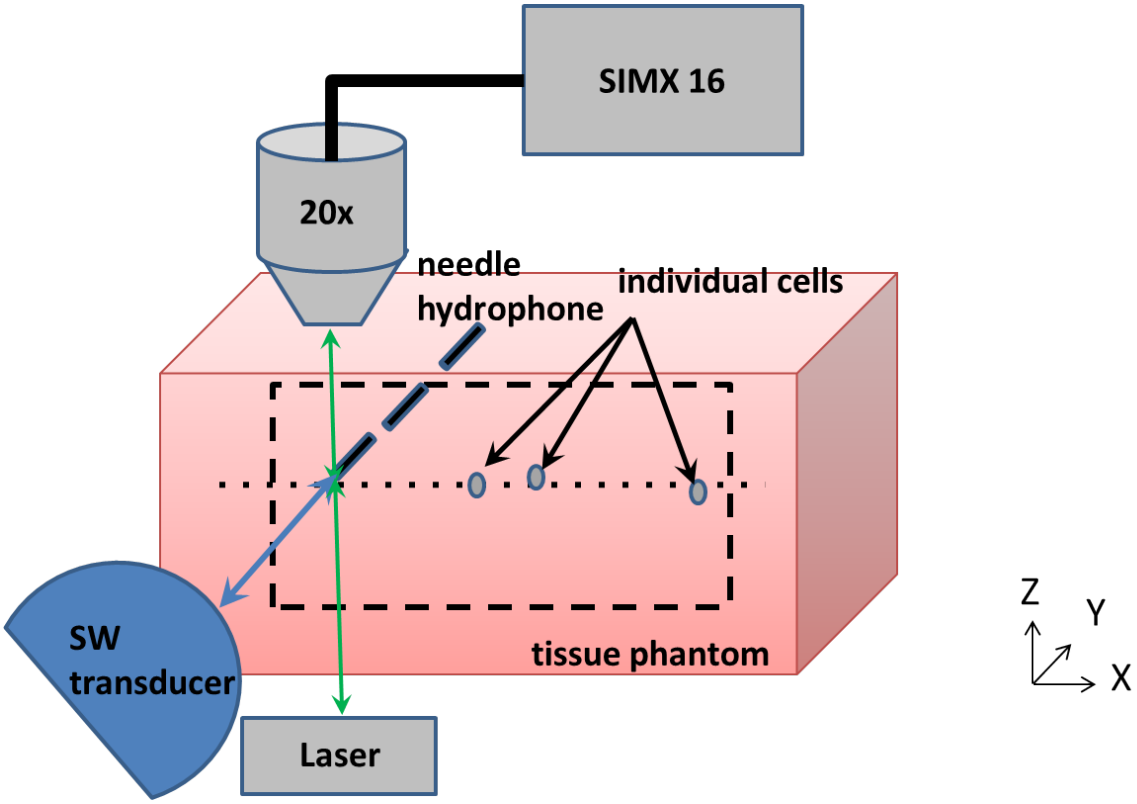

Fig. 1: Overview of the experimental setup containing a SIMX 16 ultra-high speed camera, a 20× microscopic objective, a laser source, a shock wave transducer, a needle hydrophone and a cell-agarose tissue phantom.

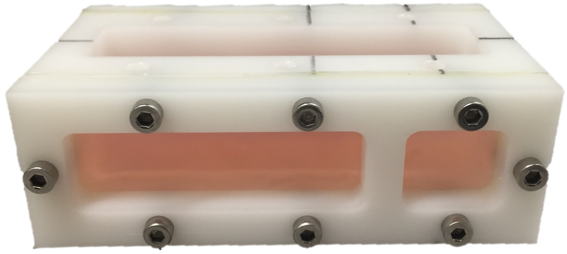

Fig. 2: Mould containing cell-agarose gel for carrying out shock wave exposure. The four transparent windows allow for imaging, lighting and applying shock waves simultaneously.

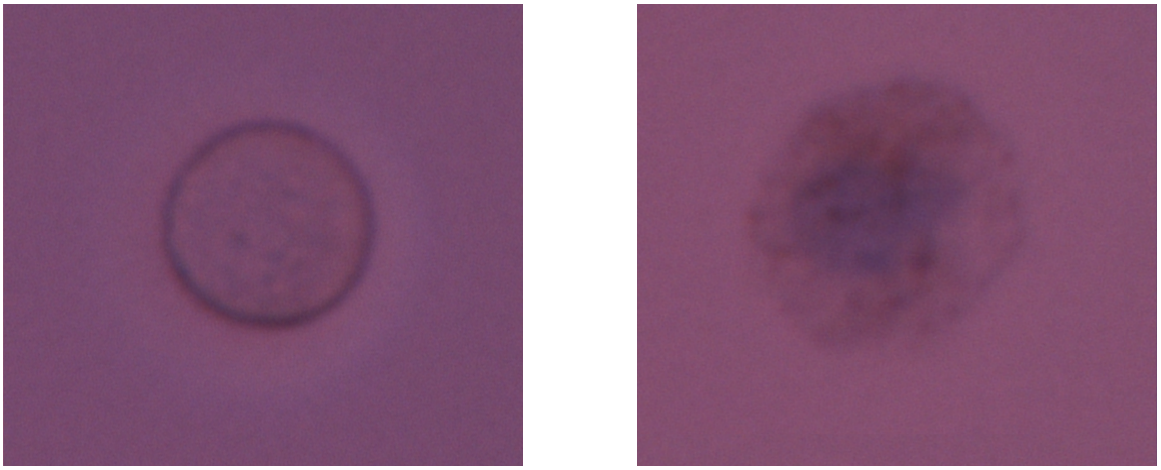

(a) (b)

Fig. 3: Examples of HK-2 cells (at 40× magnification) embedded in a 3D agarose tissue phantom: (a) a healthy cell with a well defined intact boundary; (b) a dead cell showing a diffuse boundary.

The viability of cells in the phantom was assessed by using a trypan blue solution (which selectively stains dead cells) 24 hours after they were embedded in the tissue phantom. Fig. 3(a) shows a healthy cell after 24 hours in agarose gel with a well defined boundary. In comparison Fig. 3(b) shows a cell that was non-viable, based on the blue stain, and also demonstrated a diffuse cell boundary. Fewer than 1% of cells were non-viable after 24 hours in agarose gel. The distinctive diffuse boundary was used to identify and exclude dead cells in the gel when high speed imaging was done.

1.2 Shock wave source

A clinical shock wave device (Minilith SL1-0G, Storz Medical AG) was used to generate shock waves. The Minilith employs an electromagnetic source and a parabolic reflector to effect focussing [3]. The focus occurs 50 mm from the face of the source and the focal zone is ellipsoidal in shape approximately 25 mm long in the axial direction by 2.4 mm in diameter.

Shock waves were measured inside the tissue phantoms using a fibre-optic probe hydrophone (FOPH) [4] based on a previously published design [5]. The FOPH measures light reflected from the tip of an optical fibre placed in the pressure field. As the pressure wave passes the fibre it causes a change in the refractive index of the

medium and hence changes the reflected light [5]. The FOPH employed here can measure acoustic pressures up to 100 MPa [4, 5].

The voltage output V from a photodetector is proportional to the light reflected at the fibre tip:

$$V(n) = gR(n) + S \tag{1}$$

where $R(n)$ is the reflectivity, g is the gain and S is the offset of the photodiode system (which were determined from measurements from known fluids). The reflectivity $R(n)$ is defined as:

$$R(n) = \left(\frac{n_f - n}{n_f + n}\right)^2 \tag{2}$$

where n_f is the index of refraction at the fibre (which is assumed to be constant in all conditions) and n is the index of refraction of the medium. The refractive index is related to the density through the Gladstone-Dale relation [6]:

$$\frac{n(t) - 1}{\rho(t)} = constant \tag{3}$$

With the known ambient conditions (n_0, ρ_0), the medium density can be inferred as:

$$\rho(t) = \rho_0 \frac{n(t) - 1}{n_0 - 1} \tag{4}$$

The density can be related to the pressure through the Tait equation of state,

$$p(\rho) = (Q + P_0)\left(\frac{\rho}{\rho_0}\right)^{\gamma} - Q \tag{5}$$

where $Q = 295.5$ MPa, $\gamma = 7.44$ for the conditions $T = 20$ °C, $P_0 = 100$ kPa and $\rho_0 = 1000$ kg/m^3 [5]. Therefore, using Equations (1)-(5), the pressure can be calculated from the voltage measured from the photodiode.

1.3 High speed camera and lighting source

An ultra-high speed camera (SIMX 16, Specialised Imaging) was used to image cells inside the gel. The camera has 16 CCD elements which can be triggered independently with a maximum frame rate of 200 million fps (i.e., 5 ns exposure time per frame). The camera was connected to a 20× microscopic objective (UMPLFLN20XW, Olympus) through a turning prism mirror (CM1-P01, Thorlabs) to magnify the region of interest and thus allow for close observation of a single cell (image resolution: 0.2 µm/pixel; field of view: 1.325 mm in diameter). All the connections between the microscopic objective and the camera were sealed to minimise interference from the ambient light.

The agar gel was backlit with a high speed visualisation laser (SI-LUX640, CAVITAR) which was fitted with a collimating lens. The visualisation laser was mounted onto a 3D microstage to align with the camera objective. The frame exposure time used in the experiment was 300 ns in order to observe the cell deformation as shorter times resulted in too little light to generate images of sufficient fidelity.

The camera and light source were triggered from the electromagnetic signal generated when the shock wave source was excited. For a target cells, high speed images were taken both in its reference state (i.e., before triggering shock waves) and during shock wave loading with the same imaging settings in order to measure the cell deformation in each image frame.

1.4 System alignment

The camera and shock wave source were aligned by placing a piezoelectric needle hydrophone (Müller Instruments) inside the gel coupled to the Minilith. The tissue sample was positioned such that a sharp image of the needle hydrophone was observed with the optimal light on the background. The Minilith was then manually adjusted until the pressure waveform matched a reference waveform for the focal spot. This aligned the optics and shock wave source. The gel was then translated laterally (without disturbing the position of the shock wave source or optics) until the needle was out of the region of interest and a cell could be observed. The optical system was finely adjusted (but still within the 2 mm focal spot of the shock source) to bring the cell sharply into focus.

2 Post-imaging analyses

Post-imaging analyses involved four image processing steps: image filtering, registration, automatic segmentation and feature extraction in order to determine cell boundaries. Area and perimeter measures were extracted from the cell boundary for quantitative analysis. The details of the steps are given below and the analysis was implemented in C++ and MATLAB.

2.1 Image denoising

Ultra-high speed images are generally noisy due to the low light levels, thus image filtering is desirable to allow for automatic cell contour segmentations. A non-local means (NL-means) filter [7] was applied to reduce noise while preserving the fine features of the original images. This algorithm takes advantage of the high degree of redundancy of images, i.e., images are constituted of patterns which are usually repetitive across itself [7]. Hence a noise reduced image can be reconstructed in which

the value of any pixel is estimated by all the pixels in its neighbourhood. This filtering technique is more advanced than other local smoothing methods or frequency domain filters as in the latter methods the relevant fine structures, details and texture of the original images are also smoothed out [7].

Given a noisy image v defined in a discrete gridded format I, the estimated value for pixel i is computed as a weighted average of all the pixels in the image [7]:

$$NL(v)(i) = \sum_{j \in I} w(i,j)v(j) \tag{6}$$

where the weights $w(i,j)$ depend on the similarity between the subsets around pixels i and j defined by the discrete grid:

$$w(i,j) = \frac{1}{Z(i)} e^{-\frac{\|v(N_i)-v(N_j)\|^2}{h^2}} \tag{7}$$

where the subset N_i is called the neighbourhood or similarity window of i (user-defined based on outcome quality and computational costs), $Z_i = \sum_j e^{-\frac{\|v(N_i)-v(N_j)\|^2}{h^2}}$ is the normalising factor and h is the parameter which controls the decay of the weight function.

The high speed images were firstly cropped to the region of the cell in order to improve the filter efficiency. The parameters used for the filter were optimised based on the balance between computational efficiency and filtering quality. The neighbourhood N was chosen to be 4×4 pixels, and the decay parameter $h = 100$. Fig. 4 shows an example of cell images before and after filtering. The NL-means algorithm filters out the background noise such as speckles and grids while retaining the relevant cell features.

2.2 Cell contour segmentation

The cell contour segmentation algorithm consists of an initial manual segmentation on the reference image (i.e., one of the 16 image frames taken before shock wave exposure), image registration process to propagate the initial segmentation contour to all the other high speed images, and the active contour segmentation algorithm to optimise the propagated segmentation results.

Image registration: Image registration was used to assist the process of segmentation of the cell contour on the high speed images. A high speed image sequence of a cell can be described as a set of images $I_n : \Omega \subset \mathbb{R}^2 \to \mathbb{R}$, $n \in \{1, ..., N\}$. For each of these images, there is a binary mask C_n which describes the cell contour.

Since this is a temporal sequence showing the motion of the same cell over time, it can be considered that each acquisition is equal to the first frame under a nonlinear

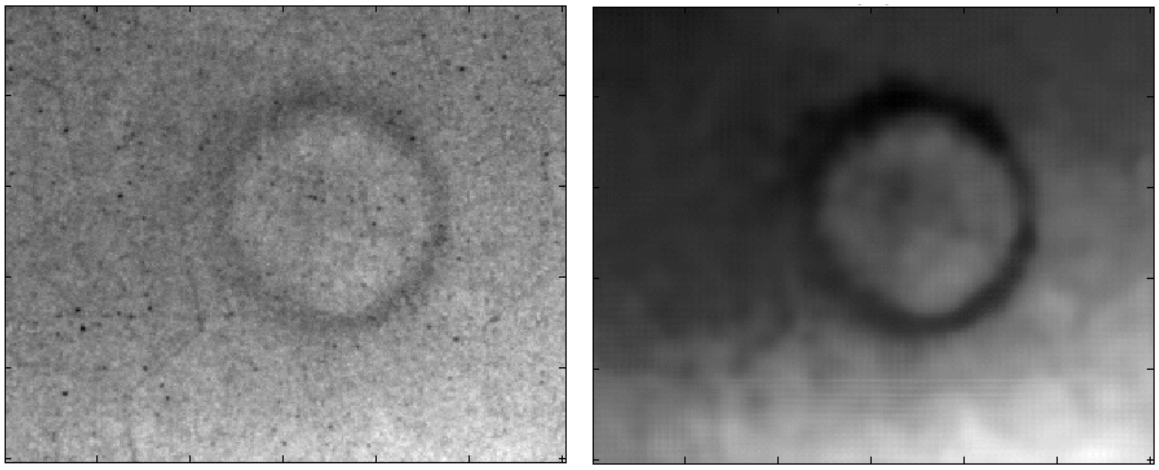

(a) (b)

Fig. 4: (a) Cropped raw image on the region of interest; (b) NL-means filtered image.

deformation field ϕ_n, an error term ϵ_n (related to noise and other artefacts), and a spatially varying multiplicative term K_n for illumination changes:

$$I_n = (I_1 K_n + \epsilon_n) \circ \phi_n \tag{8}$$

where $\circ$ is the operator that applies such deformation field. Consequently, given a contour for the first acquisition C_1, each subsequent contour is given by: $C_n = C_1 \circ \phi_n$. Image registration is used to estimate each of these deformation fields and hence propagate the initial contour to all frames. Its basic concept is to identify the optimal deformation field $\hat{\phi}_n$ based on an error metric E:

$$\hat{\phi}_n = \arg\min_{\phi_n} [E(I_1 \circ \phi_n, I_n)] \tag{9}$$

In this work, image registration was used to estimate the deformation fields and the estimation of the cell contours on image n was taken to be: $\hat{C}_n = C_1 \circ \hat{\phi}_n$.

The error measure E attempts to quantitatively evaluate the misalignment of both images, the most basic metric is the sum of square differences. However, the large changes of contrast in the images over the time sequence severely hinders its use as a measure of similarity for this problem. A similar challenge is found on liver ultrasound sequences, where occlusions lead to high contrast variability. For such case, the Scale Invariant Feature Transform (SIFT) has been used as similarity metric to great success [8]. It extracts features based on the gradient orientation profile of quadrants around each pixel of the images. These features are robust to illumination changes and are able to capture the main structural characteristics of the images.

The local mean square error of the feature vectors at each voxel can then be used as a robust measure of similarity.

The motion on the cells is expected to be smooth and without folding, hence, ϕ_n should be restricted to such deformation fields. Here we applied a logDemons framework which ensures that the obtained transformation fields are diffeomorphic, and thus satisfying the restrictions on the smooth deformation fields (no folding) [9]. It was combined with SIFT as a similarity metric in a multi-resolution application. It used three resolution levels, with 20 iterations at each level. The transformation field was smoothed at each iteration with $\sigma_{\text{diff}} = 2$ pixels. The SIFT Flow library was used for dense SIFT with its default parameters [10].

Active contour segmentation: Cell contours in each high speed image sequences were refined automatically using an active contour segmentation [11]. Any segmentation that was unsuccessful or visually unsatisfactory was then segmented manually with three repeats. An initial guess of the cell contour obtained from the initial manual segmentation and the image registration algorithm served as the input to the active contour segmentation algorithm. The active contour segmentation is an energy-minimising spline influenced by the image features and constrained by external forces which are user-defined in order to achieve the best contour segmentation results.

2.3 Feature extraction and analysis

The projected cell area, perimeter and centre of mass were determined from the cell contour segmentations, see Fig. 5. The cell area was estimated by counting the number of pixels within the cell contour and the cell perimeter was evaluated by summing up the distance between adjacent pixels on the contour.

Normalised area and perimeter changes at each imaging time point were defined by dividing the area or perimeter difference by their initial values at the reference state (i.e., before shock wave exposure), A_0 and P_0:

$$\begin{aligned} \frac{\Delta A}{A_0} &= \frac{A(t) - A_0}{A_0} \\ \frac{\Delta P}{P_0} &= \frac{P(t) - P_0}{P_0} \end{aligned} \tag{10}$$

where $A(t)$ and $P(t)$ are the measurements of area and perimeter respectively during shock wave exposure at time t. The shearing related perimeter change which excludes the effect of area change, $\Delta P_s(t) = P(t) - P_A(t)$, was analysed by comparing the deformed perimeter, $P(t)$, during shock waves to P_A, the expected perimeter change

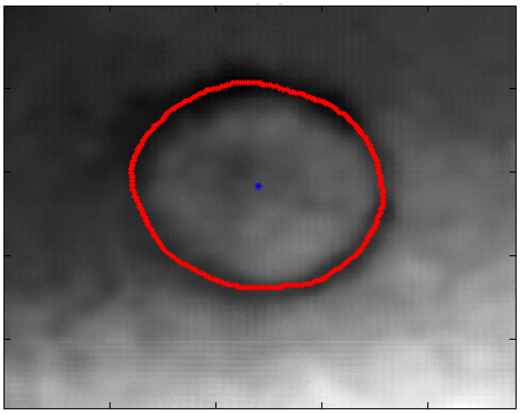

Fig. 5: An example of segmented cell showing the contour (red line) and centre of mass (blue dot).

due to the influence of area change for a circle:

$$P_A(t) = P_0\sqrt{\frac{A(t)}{A_0}} \tag{11}$$

Fig. 6 shows the relative shear perimeter change for the three cell types at all shock wave energy levels, revealing a value of less than 0.5%. This indicates that the perimeter change due to shearing was not detectable compared to the volumetric influence.

The image processing procedures described above are summarised in Fig. 7.

2.4 Segmentation variability

In order to quantify the variability in the segmentation process, a test was conducted on eight different cells per cell line subjected to shock waves with the three energy levels respectively. Each cell was manually segmented three times. The image processing algorithms were then performed on each manual cell segmentation in order to compare the measured area in each segmentation. The segmentation variability was defined as the variation of the measured area in the three segmentations. The test was repeated for each cell sample per cell line. Fig. 8 shows the segmentation variability of the three cell lines measured at shock wave energy level 8 where the greatest variance was found. In all cell samples the maximum area variability for the segmentation prior to the arrival of the shock waves was less than 0.2%. During shock loading, the majority of the cell samples exhibited less than 1% variability. In a few

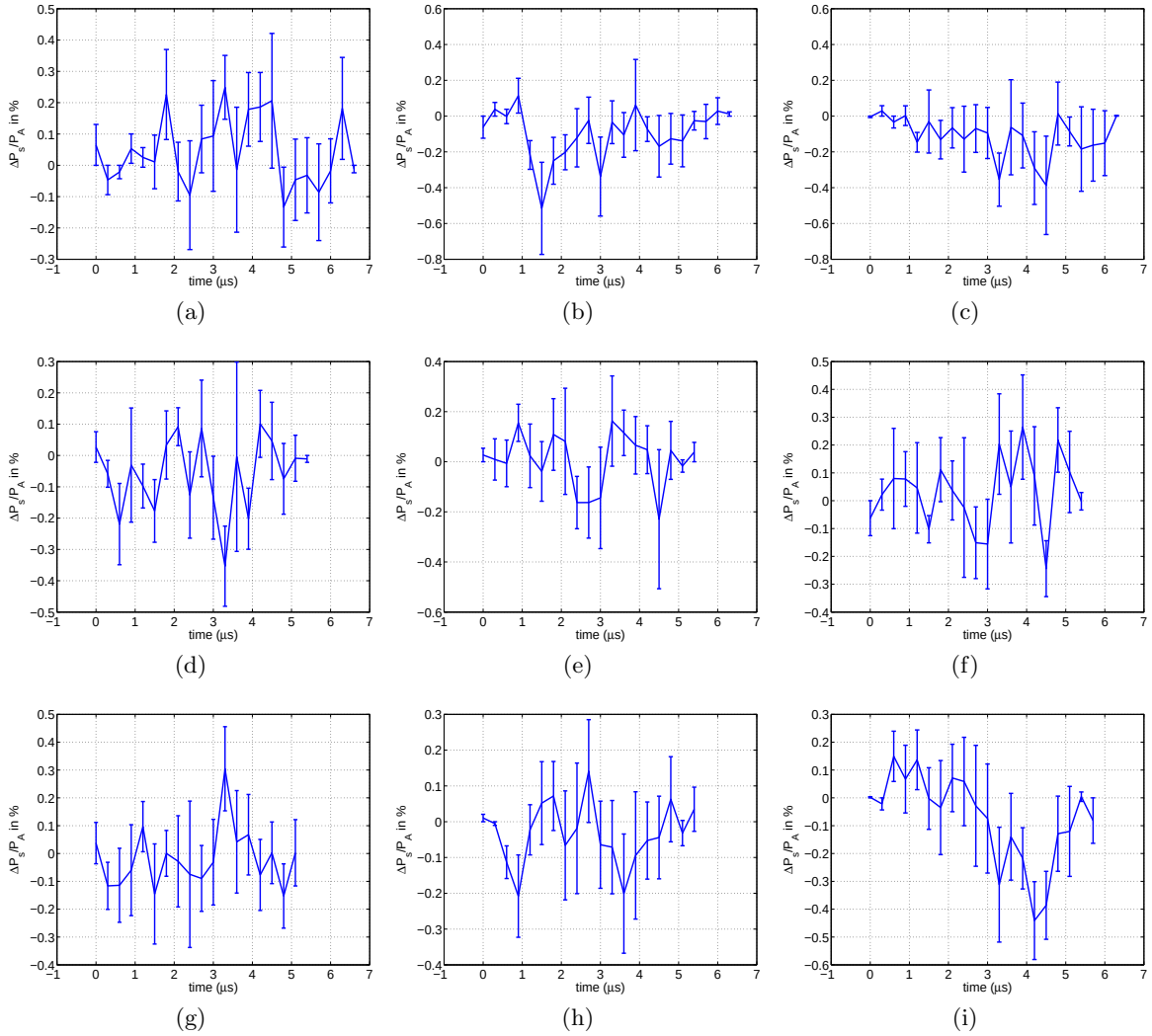

Fig. 6: The shear-related perimeter change for the three cell types: (a)-(c) HRE cells, (d)-(f) HK-2 cells, (g)-(i) CAKI-2 cells, at shock wave energy level 4 (a)(d)(g), 6 (b)(e)(h) and 8 (c)(f)(i).

cases a variability of 2-5% occurred during stretching, due to reduced image quality and thicker cell contours during the tensile phase of shock wave exposure.

2.5 Imaging variability

During the imaging process, the movement of the cells and the interaction between acoustics and optics may result in artefacts or interference in cell images leading to cell

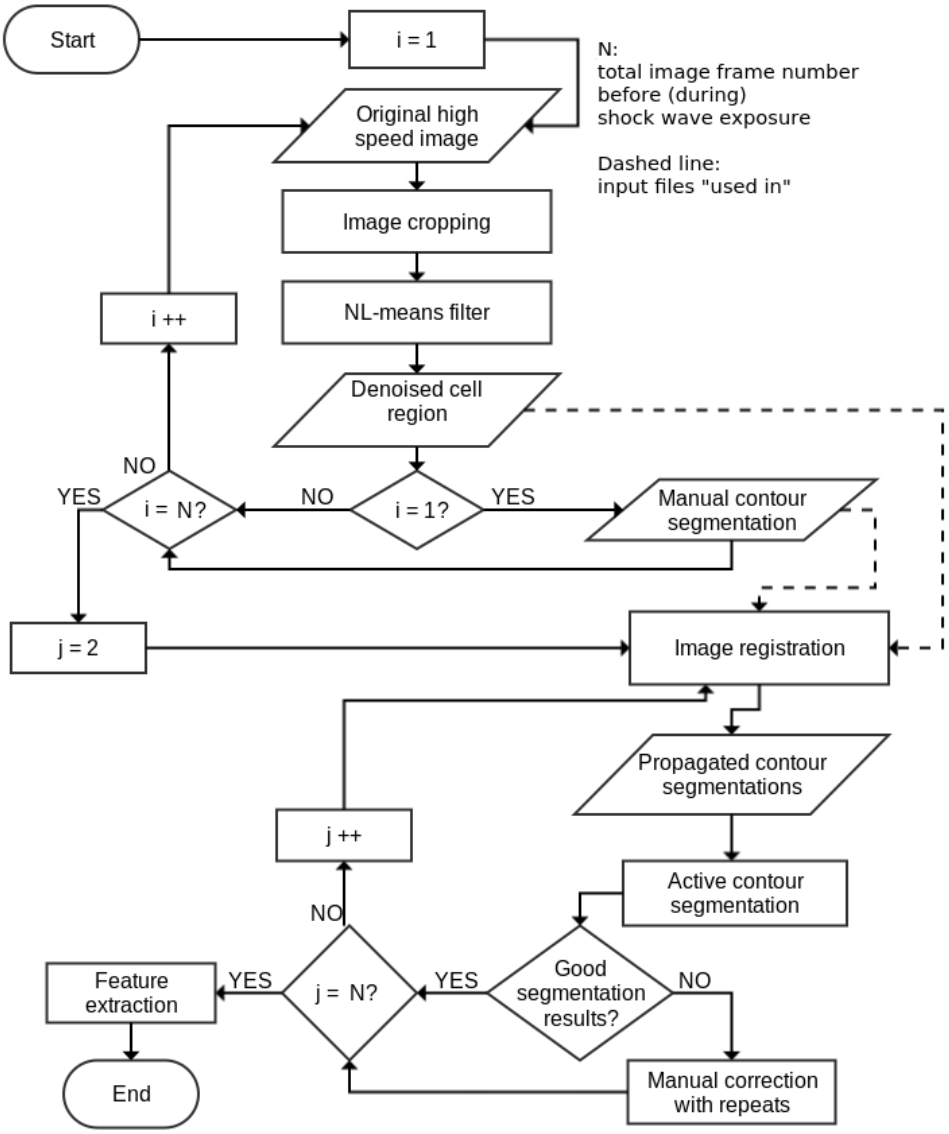

Fig. 7: Summary of the main procedures of cell image postprocessing.

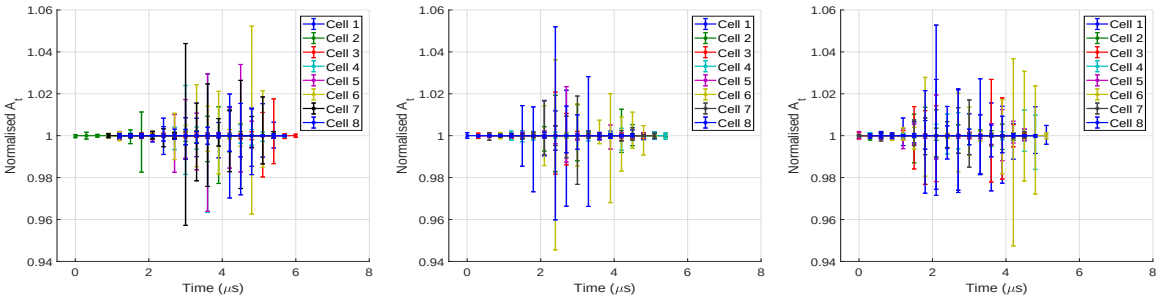

(a) (b) (c)

Fig. 8: The minimum and maximum segmented areas relative to the mean value of 8 cell samples taken at shock wave energy level 8 in (a) HRE cells; (b) HK-2 cells and (c) CAKI-2 cells.

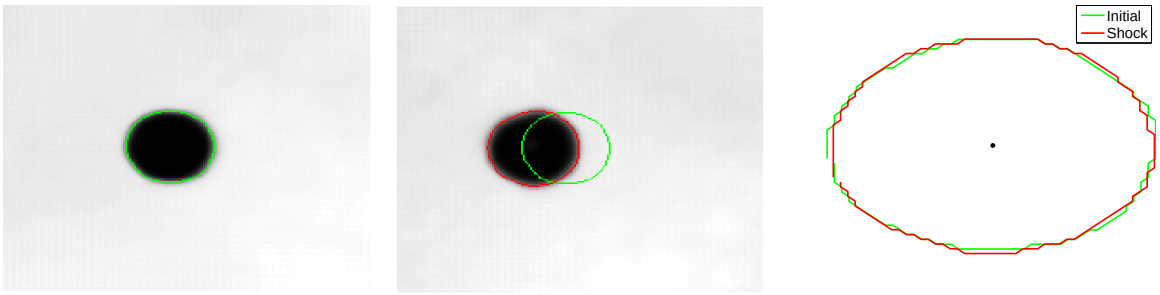

(a) (b) (c)

Fig. 9: An example of segmented microbeads at shock wave energy level 8. (a) before shock wave exposure; (b) during shock wave loading; (c) contour comparison.

contour change which is not due to the cell deformation in response to shock waves. Therefore, 10 µm polystyrene microspheres (Polybead, black, Polyscience Inc.) were used in the same experimental setting and post-imaging analysis was carried out in the same manner as for the cells. Due to the large bulk modulus of the microbeads (∼4 GPa [12]), shock waves should not lead to a detectable area change of the beads. Therefore, they can be used to assess the influence of acousto-optic effects, bead and gel movement, and image quality on the cell images.

Representative images and the segmentation of a microbead are presented in Fig. 9, it can be seen that the bead is translated but there is no significant change in its contour during shock wave exposure.

The area changes of the microbead contour measured at the three shock wave energy levels are presented in Fig. 10. The results showed that the area change of

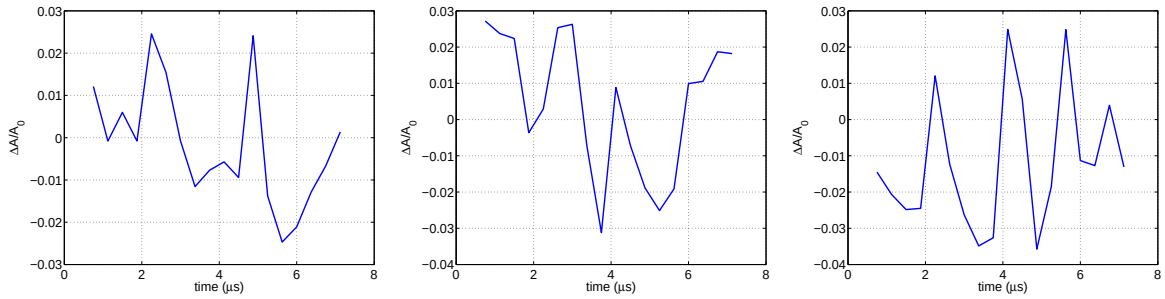

(a) (b) (c)

Fig. 10: Area change of the microbead contour at different shock wave energy levels (a) level 4; (b) level 6; and (c) level 8.

the 10 µm microbeads varied between -3% and 3% at the three shock wave energy levels. The mean error of area change found in the three shock wave energy levels (levels 4-8) were 0.1%, 0.4% and -1.1%, respectively. The area change of microbeads does not show a correlation with the shock wave profile whilst that of cells showed clear negative and positive phases of area change consistent with the compressive and tensile portions of the shock wave. This indicates that the imaging variability of microbeads may not be caused by shock wave interactions but the small movement of the objects inside the gel and segmentation variability.

3 Experimental results of cell deformation

Fig. 11 shows the maximum area increase changing with the shock wave energy levels: at energy level 4, the area increase in all three cell lines was found to be between 3.3% and 4.1%; at shock wave energy level 6, the area increase was between 6.3% and 8.5%; and at energy level 8, the maximum area increase was 17% in the HK-2 cells, 13% in HRE and 9% in CAKI-2. The difference was statistically significant for HK-2 and CAKI-2 cells with a p-value of less than 5% in the Mann-Whitney U test.

As a circle changes in radius from an initial radius r_0 to a different radius r_t, the area and perimeter are given by:

$$\begin{aligned} \frac{\Delta A}{A_0} &= \frac{2\pi\left(r_t^2 - r_0^2\right)}{2\pi r_0^2} \simeq \frac{4\pi r_0 \Delta r}{2\pi r_0^2} = \frac{2\Delta r}{r_0} \\ \frac{\Delta P}{P_0} &= \frac{2\pi\left(r_t - r_0\right)}{2\pi r_0} = \frac{\Delta r}{r_0} \end{aligned} \tag{12}$$

The ratio of the area change to perimeter change would therefore be a factor of two. Under the same area change, assuming the circle is gradually deforming to an ellipse,

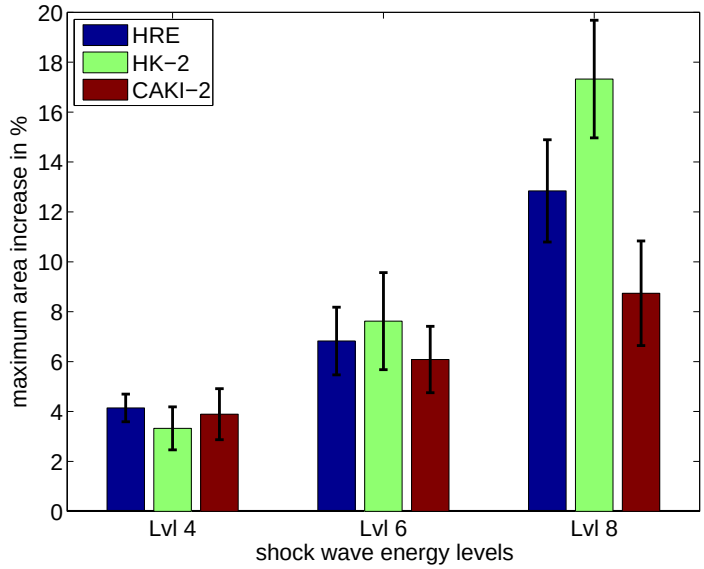

Fig. 11: The maximum area increase for the three cell types at three shock wave energy levels: (blue) HRE cells; (green) HK-2 cells and (red) CAKI-2 cells.

the area change over perimeter change is presented in Fig. 12, where b and a are the major and minor axes of an ellipse. For an ellipse with more than 10% axes length difference, the relative area change over relative perimeter change is less than 1.5.

Fig. 13 shows the ratio of the projected area change to perimeter change for all three cell types at the three different energy level settings. The ratio remained between 1.5 and 2 shows an axes difference less than 10% for an ellipse and suggests that the cells did not undergo substantial shear deformation during the shock wave exposure.

4 Cell viability test

A lactate dehydrogenase (LDH) assay was used to quantify cell viability inside the agarose gel. LDH is a cytosolic enzyme present in many different cell types. Cell membranes damaged by shock waves thus release LDH into the surrounding cell medium, which in turn can be quantified through enzymatic reaction and colorimetric detections. The level of LDH detected is directly proportional to cell damage, which indicates cell cytotoxicity [13]. In order to have sufficient cell density for the assay, the original sample mould (Fig. 1) was modified to concentrate cell populations to the shock wave focal zone in three cylindrical compartments (16 mm in diameter and 10 mm in height), see Fig. 14. Each compartment was filled with ∼500,000 cells homogenously embedded in the agarose gel with the same consistency as the rest of the tissue-mimicking phantom (0.6% agarose).

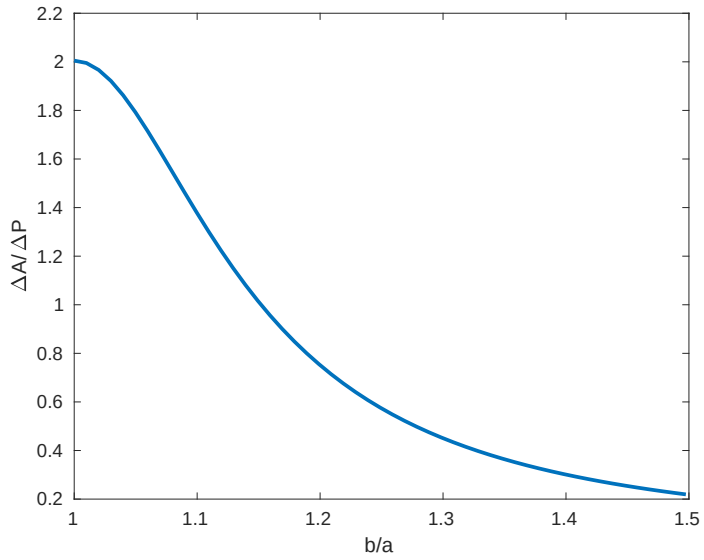

Fig. 12: The ratio of area change over perimeter change, where b/a is the ratio of the major over minor axis of an ellipse.

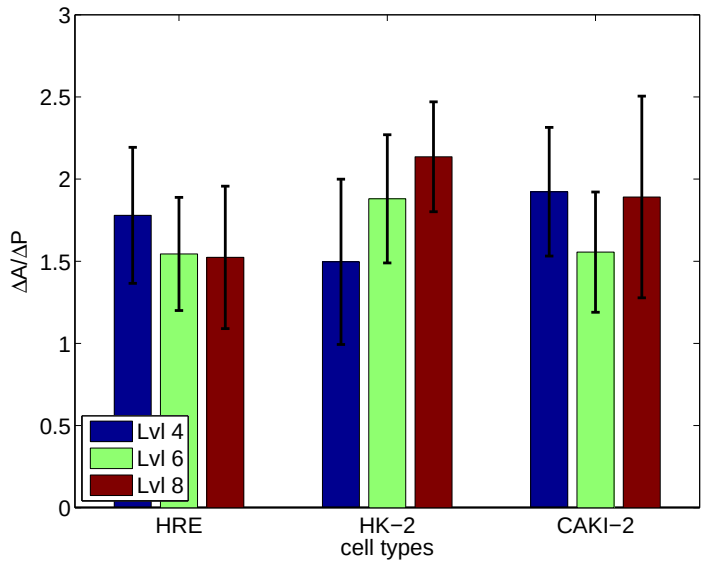

Fig. 13: The ratio between area change and perimeter change of single cell deformation in response to shock waves for the three cell lines: (blue) level 4; (green) level 6 and (red) level 8.

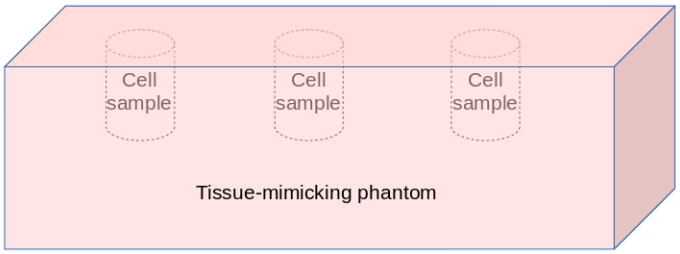

Fig. 14: Schematic of cell viability test samples.

The cell samples were treated with 500 shock waves at shock wave energy levels 4 and 8. At the same time, maximum LDH release control and sham control were included. A maximum LDH release control that represents the maximum cell cytotoxity was determined by lysing the cell sample before the gel set, while the sham control representing the maximum cell viability was determined by keeping the cell sample in the 37 °C incubator without shock wave treatments. The protocol is modified from reference [14].

After the shock wave treatments, the cell samples were carefully disected from the tissue phantom and placed in a 12-well plate filled with 2 mL cell medium. A complete medium control with only cell growth medium, no cells, was used to determine the background LDH activity due to the cell medium. The well plate was placed in the 37 °C incubator for 18 hours to allow the LDH to diffuse into the cell medium. Subsequently, 50 µL samples of the medium were collected from each well into a 96-well plate for LDH analysis using a LDH cytotoxicity assay kit (Pierce, ThermoFisher Scientific). The assay was performed by transferring 50 µL of reaction mixture to each sample well and mixing by gentle tapping. After incubating the plate at room temperature protected from light for 30 min, 50 µL stop solution was added to each sample well. The absorbance at 490 nm and 680 nm was measured using the FLUOstar Omega micro-plate reader to determine the LDH activity. The cell cytotoxicity was calculated as:

$$\%cytotoxicity = \frac{D_{sample} - D_{sham}}{D_{maxrelease} - D_{sham}} \times 100 \tag{13}$$

where D represents the absorbance measured at 490 nm subtracted from that at 680 nm.

5 Numerical modelling

5.1 Model geometry

Fig. 15 shows the 3D Finite Element model, which consists of a cell model of 20 µm in diameter embedded in a tissue model describing the surrounding extracellular matrix.

The shock wave profiles measured in the experiment were applied at the top surface

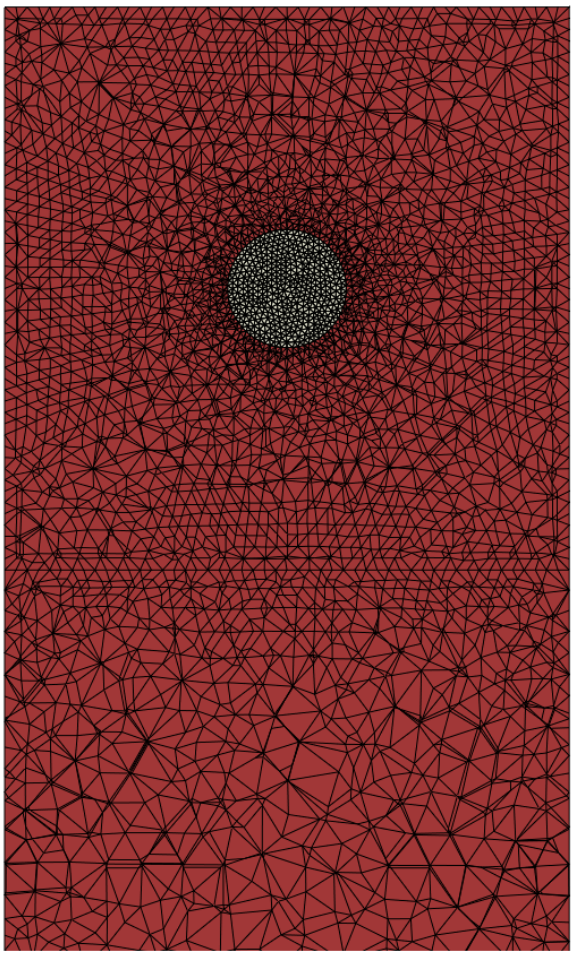

Fig. 15: Cross-sectional view from the mid-plane of the FE model (bottom truncated for presentation): a cell embedded in the surrounding tissue model.

of the model as an incident plane wave. The lateral boundaries were prohibited from moving laterally, and the bottom was fixed. The cell was positioned 50 µm from the top surface to minimise losses in the propagation of the incident wave, and the overall model length was taken to be 5 mm to ensure that wave reflections from the bottom boundary occurred only after the shock wave tail fully crossed the cell.

5.2 Constitutive framework

The conservation of linear momentum of a continuum system is described by:

$$\nabla \mathbf{P} + \rho_0 \mathbf{b} = \rho_0 \ddot{\mathbf{x}}, \qquad \forall \mathbf{X} \in B_0 \tag{14}$$

where $\mathbf{P}$ is the first Piola-Kirchhoff stress tensor which effectively relates force in the deformed configuration to area in the reference (undeformed) configuration B_0, ρ_0 is the density in B_0, $\mathbf{b}$ is the body force vector per unit mass, and $\mathbf{X}$ and $\mathbf{x}$ are the point coordinates vector in the reference and deformed configuration respectively.

The determination of the stress measure is also related to the deformation of the material of interest through its constitutive material law. The second Piola-Kirchhoff stress $\mathbf{S} = \mathbf{F}^{-1}\mathbf{P}$ and the Kirchhoff stress $\boldsymbol{\tau} = \mathbf{P}\mathbf{F}^T$ are also used in the description of the material laws. Here, $\mathbf{F} = \frac{\partial \mathbf{x}}{\partial \mathbf{X}}$ is the deformation gradient tensor and $J = det\,(\mathbf{F})$ is the Jacobian which represents the volumetric change with respect to the reference configuration. The cell deformation in the model was decomposed into a deviatoric response and a volumetric response, which are described below.

Nonlinear viscoelasticity: The deviatoric material response was described by a nonlinear viscoelasticity framework [15], where the deviatoric second Piola-Kirchhoff stress $\bar{\mathbf{S}}$ of the viscoelastic system (see Fig. 16) depends on the deviatoric initial elastic response $\bar{\mathbf{S}}^{\circ}$ and the evolution of the stress-like viscous internal variables $\mathbf{Q}_i$:

$$\bar{\mathbf{S}}(t) = \bar{\mathbf{S}}^{\circ}(t) - J^{-\frac{2}{3}}\mathrm{DEV}[\sum_{i=1}^{N} \mathbf{Q}_i(t)] \tag{15}$$

where N is the number of viscoelastic branches in Fig. 16; $N = 1$ for the first order generalised Maxwell viscoelastic model.

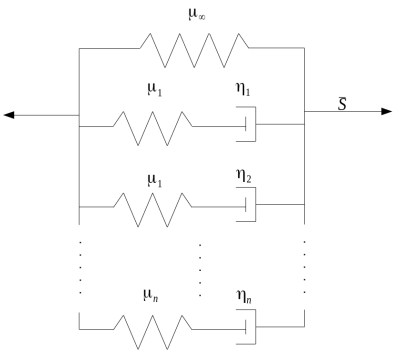

Fig. 16: Schematic of the viscoelasticity material framework in small deformation [15]

The deviatoric initial elastic stress is the derivative of the volume-preserving elastic stored energy function $\bar{W}^{\circ}$ with respect to the deviatoric right Cauchy-Green tensor $\bar{\mathbf{C}} = \bar{\mathbf{F}}^T\bar{\mathbf{F}}$ [15]:

$$\bar{\mathbf{S}}^{\circ}(t) = J^{-\frac{2}{3}}\mathrm{DEV}\{2\partial_{\bar{\mathbf{C}}}\bar{W}^{\circ}[\bar{\mathbf{C}}(t)]\} \tag{16}$$

where the operator "DEV" provides the correct notion of "deviatoric" stress tensor in terms of the right Cauchy-Green tensor $\mathbf{C}$, satisfying: $\mathbf{C}$**:**$\mathrm{DEV}[\bullet] = 0$.

The evolution of the internal variables is extended from the linear (small deformation) viscoelasticity case:

$$\begin{cases} \dot{\mathbf{Q}}_i(t) + \dfrac{1}{\tau_i}\mathbf{Q}_i(t) = \dfrac{\gamma_i}{\tau_i}\mathrm{DEV}\{2\partial_{\bar{\mathbf{C}}}\bar{W}^{\circ}[\bar{\mathbf{C}}(t)]\} \\ \lim\limits_{t\to\infty}\mathbf{Q}_i = \mathbf{0} \end{cases} \tag{17}$$

where $\tau_i = \eta_i/\mu_i$ is the relaxation time of each viscoelastic component and γ_i is the ratio of the shear modulus of each viscous component to the instantaneous shear modulus (i.e., $\gamma_i = \mu_i/\mu_0$).

After a few manipulations, the deviatoric Kirchhoff stress $\bar{\boldsymbol{\tau}}$ is given by:

$$\begin{aligned} \bar{\boldsymbol{\tau}}(t) =& \gamma_{\infty}\mathrm{dev}\{2\partial_{\bar{\mathbf{C}}}W^{\circ}[\bar{\mathbf{C}}(t)]\} \\ &+ \sum_{i=1}^{N}\gamma_i\mathrm{dev}\{\bar{\mathbf{F}}(t)\int_{-\infty}^{t}\exp[-(t-s)/\tau_i]\frac{d}{ds} \\ &\bar{\mathbf{F}}(s)^{-1}\mathrm{dev}\{2\partial_{\bar{\mathbf{C}}}\bar{W}^{\circ}[\bar{\mathbf{C}}(s)]\bar{\mathbf{F}}(s)^{-T}\}ds\bar{\mathbf{F}}(t)^T\} \end{aligned} \tag{18}$$

where "dev" is the deviator operator defined by: $\mathrm{dev}[\bullet] = (\bullet) - \frac{1}{3}[(\bullet):\mathbf{I}]\mathbf{I}$.

Equation of state: The volumetric Kirchhoff stress is given by $\boldsymbol{\tau}^{\circ}_{vol} = Jp\mathbf{I}$, where the pressure p captures the difference in bulk modulus under compression and tension. During compression the bulk modulus is taken to be K_C but during tension when the pressure exceeds the transition pressure threshold, $\tilde{p}$, the bulk modulus reduces to K_T (see Fig. 17):

$$\begin{aligned} p =& \mathrm{H}(\widetilde{p} - p)\left(K_T\frac{\rho-\rho_0}{\rho_0} + \Delta p\right) \\ &+ \mathrm{H}(p-\widetilde{p})\left(K_C\frac{\rho-\rho_0}{\rho_0}\right) - K_C\frac{\widetilde{\rho}-\rho_0}{\rho_0} \end{aligned} \tag{19}$$

where H is the Heaviside function, $\Delta p = (K_C - K_T)(\widetilde{\rho}-\rho_0)/\rho_0$, $\widetilde{p}$ and $\widetilde{\rho}$ are the transition pressure and density, respectively. The compressive bulk modulus K_C was determined to be 2 GPa due to small cell deformation under compression and high

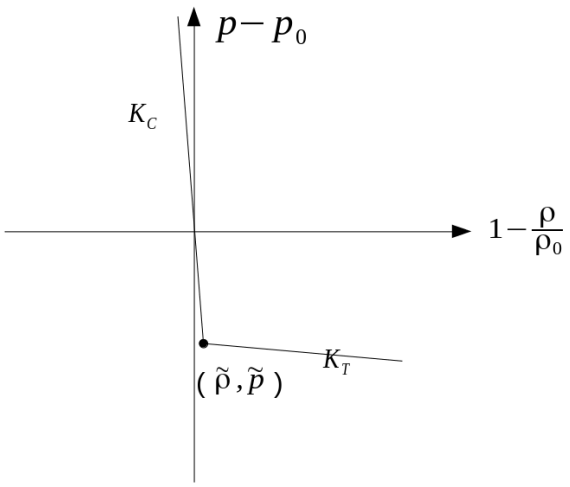

Fig. 17: Schematic of the bilinear EoS accounting for different bulk moduli for the compressive (K_C) and tensile phases (K_T) of shock waves. $\tilde{\rho}$ and $\tilde{p}$ are the density and pressure at the transition, and p_0 and ρ_0 refer to their reference states.

water content of the cell, whilst the other parameters (K_T and $\tilde{p}$) were calibrated against experimental observations.

Artificial viscosity: In a discretised scheme, such as in the finite element method, artificial viscosity is necessary to spread the shock front over several elements so that the simulation of shock fronts (with length scale a prori less than the mesh size) can be captured without introducing spurious oscillations. The spurious oscillations can be eliminated by subtracting a certain amount of pressure p_{av} from the original pressure loadings [16], where p_{av} is expressed as:

$$p_{av} = \rho l_e \dot{\epsilon_v} (b_1 c_d + l_e {b_2}^2 \dot{\epsilon_v}) \tag{20}$$

where b_1 and b_2 are the linear and quadratic damping coefficients, respectively, l_e is the characteristic element size, $\dot{\epsilon_v}$ is the volumetric strain rate and c_d is the longitudinal wave (p-wave) speed.

5.3 Numerical model calibration and validation

The material properties (K_T and $\tilde{p}$) in the constitutive framework of each cell model were calibrated against the experimental data by finding the least mean square error between the simulation and experimental results in terms of the area change for all the three shock wave loading conditions. This process was cross-validated by determining the optimal values for only two of the energy level settings at a time and testing for the

"left out" (untrained) energy setting by analysing the difference between its simulation and experimental results using the previously calibrated values. Table 1 lists the cross-validation results for each cell line, including different training combinations, resultant calibration values and error between simulation and experimental results in the untrained data set. The calibration process of the numerical model presents an error around 12% for all cell types, which is acceptable considering the small compressive deformation and the experimental variation, see Fig. 3 in the main article. It can also be seen that the transition pressure values obtained for healthy (HRE and HK) cells are consistently larger in magnitude compared to that of cancer (CAKI) cells. This indicates a physical difference in transition pressure between two groups which is highlighted by performing a Welch's t-test with a p value less than 0.1.

Table 1: Cross-validation of the numerical model for the three cell lines.

Cell type	Trained settings	Optimal properties		Untrained setting	error	mean error
		K_T	$\tilde{p}$			
HRE	Lvl 4 & Lvl 6	20MPa	-4.6MPa	Lvl 8	6.8%	
	Lvl 4 & Lvl 8	25MPa	-4.4MPa	Lvl 6	17.9%	
	Lvl 6 & Lvl 8	20MPa	-5.2MPa	Lvl 4	12.4%	12.4%
HK	Lvl 4 & Lvl 6	20MPa	-4.6MPa	Lvl 8	7.7%	
	Lvl 4 & Lvl 8	20MPa	-4.6MPa	Lvl 6	9.5%	
	Lvl 6 & Lvl 8	19MPa	-4.4MPa	Lvl 4	19.8%	12.3%
CAKI	Lvl 4 & Lvl 6	22MPa	-4.4MPa	Lvl 8	13.7%	
	Lvl 4 & Lvl 8	35MPa	-4MPa	Lvl 6	8.1%	
	Lvl 6 & Lvl 8	35MPa	-3.8MPa	Lvl 4	14.1%	12.0%

5.4 Quantification of stress and strain evolution of cells

Fig. 18 shows the comparison of the simulated pressure waveforms obtained at the centre of each cell model at the three shock wave energy levels. The maximum pressure differences among the three cell lines were 7%, 3% and 5% corresponding to shock wave energy level 4, 6 and 8, respectively. This shows that the shock wave propagation is not strongly influenced by the difference in mechanical properties between the cell types. The maximum von Mises stress, which quantifies the amount of shearing in the model, was found to be of the order of 100 Pa measured at the cell equator using the deviatoric mechanical properties from the literature.

The membrane strain in each cell line at different shock wave energy levels is depicted in Fig. 19. The membrane strain is defined by the ratio of the difference in

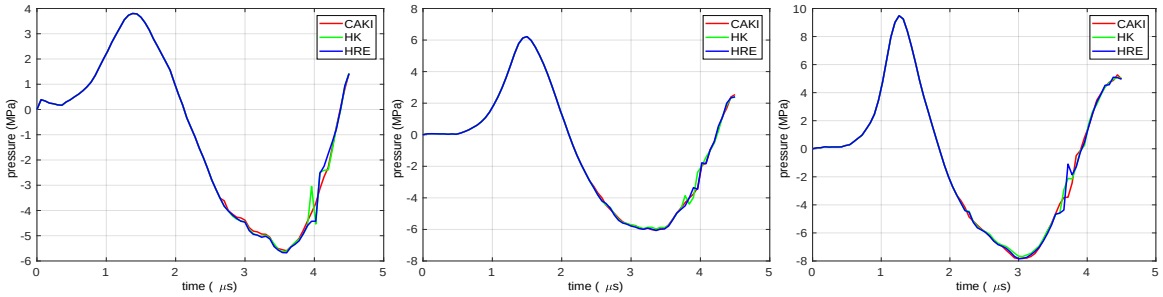

(a) (b) (c)

Fig. 18: Comparison of the simulated pressure measured in the centre of the cell models: (a) level 4; (b) level 6; (c) level 8; CAKI-2 cells (red); HK-2 (green) and HRE (blue).

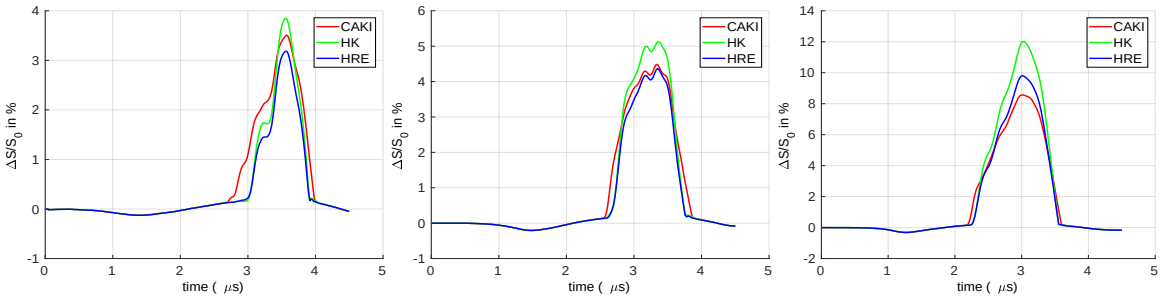

(a) (b) (c)

Fig. 19: The overall simulated cell membrane strain: (a) level 4; (b) level 6; (c) level 8; CAKI-2 cells (red); HK-2 (green) and HRE (blue).

the cell membrane surface area to the initial value at the reference state, S_0:

$$\frac{\Delta S}{S_0} = \frac{S(t) - S_0}{S_0} \tag{21}$$

where $S(t)$ is the surface area of the cell membrane during shock wave exposure at time t. The results show greater variation than the pressure waveforms. The maximum membrane area expansion under tension reached up to 10% in HRE, 12% in HK-2 and 8.5% in CAKI-2 cells at shock wave energy level 8.

References

1. G. E. Leclerc, L. Debernard, F. Foucart, L. Robert, K. M. Pelletier, F. Charleux, R. Ehman, and H. B. Tho, "Characterization of a hyper-viscoelastic phantom mimicking biological soft tissue using an

abdominal pneumatic driver with magnetic resonance elastography (mre)," *Journal of Biomechanics*, vol. 45, no. 6, pp. 952–957, 2012.
2. S. F. Bensamoun, L. Robert, G. E. Leclerc, L. Debernard, and F. Charleux, "Stiffness imaging of the kidney and adjacent abdominal tissues measured simultaneously using magnetic resonance elastography," *Clinical Imaging*, vol. 35, no. 4, pp. 284–7, 2011.
3. O. Wess, *Extracorporeal Shock Wave Therapy (ESWT) in Orthopaedics and Traumatology. User Manual.*
4. M. R. Betney, R. A. Roy, and Y. Ventikos, "Computational and experimental study of intense shock-cavity interactions," Ph.D. dissertation, University of Oxford, 2015.
5. J. Parsons, C. Cain, and J. B. Fowlkes, "Cost-effective assembly of a basic fiber-optic hydrophone for measurement of high-amplitude therapeutic ultrasound fields," *The Journal of the Acoustical Society of America*, vol. 119, no. 3, pp. 1432–40, 2006.
6. J. H. Gladstone and T. P. Dale, "Researches on the refraction, dispersion, and sensitiveness of liquids," *Philosophical Transactions of the Royal Society of London*, vol. 153, no. 1863, pp. 317–343, 1863.
7. A. Buades, B. Coll, and J. M. Morel, "A review of image denoising algorithms, with a new one," *Society of Industrial and Applied Mathematics*, vol. 4, no. 2, pp. 490–530, 2005.
8. A. Hallack, B. W. Papiez, A. Cifor, M. J. Gooding, and J. A. Schnabel, "Robust liver ultrasound tracking using dense distinctive image features," in *Challenge on Liver Ultrasound Tracking CLUST 2015*, 2015.
9. T. Vercauteren, X. Pennec, A. Perchant, and N. Ayache, "Symmetric log-domain diffeomorphic registration: a demons-based approach," *MICCAI*, 2008.
10. C. Liu, J. Yuen, and A. Torralba, "SIFT flow: Dense correspondence across scenes and its applications," *IEEE Transactions on Pattern Analysis and Machine Intelligence*, vol. 33, no. 5, 2011.
11. M. Kass, A. Witkin, and D. Terzopoulos, "Snakes - active contour models," *International Journal Of Computer Vision*, pp. 321–331, 1987.
12. P. Mott, J. Dorgan, and C. Roland, "The bulk modulus and poisson's ratio of incompressible materials," *Journal of Sound and Vibration*, vol. 312, no. 4-5, pp. 572–575, 2008.
13. Thermo Scientific, *Pierce LDH Cytotoxicity Assay Kit, User Manual.*
14. S. Nwokeoha, "Lithotripter shock wave induced rna-based gene therapy," Ph.D. dissertation, University of Oxford, 2018.
15. J. Simo and T. Hughes, *Computational inelasticity.* Springer, 2008.
16. *Abaqus user manual 6.12*, 2012.